CHALMERS
UNIVERSITY OF TECHNOLOGY

Effect of the powder feedstock on the oxide dispersion strengthening of 316L stainless steel produced by laser powder bed fusion

Materials Characterization 169 (2020) 110582

Contents lists available at ScienceDirect

Materials Characterization

journal homepage: www.elsevier.com/locate/matchar

Effect of the powder feedstock on the oxide dispersion strengthening of 316L stainless steel produced by laser powder bed fusion

Dmitri Riabov[a,c,*], Masoud Rashidi[a,b], Eduard Hryha[a], Sven Bengtsson[c]

[a] Industrial Materials and Science, Chalmers University of Technology, Gothenburg 412 96, Sweden
[b] Mechanical and Aerospace Engineering, Nanyang Technological University, Singapore 639798
[c] Höganäs AB, Höganäs 263 39, Sweden

ARTICLE INFO

Keywords:
Additive manufacturing
316L
ODS
L-PBF
Water atomized powder
Oxides
Oxide transformation

ABSTRACT

In this study, the concept of enhancing the in-situ oxide precipitation in laser powder-bed fusion processed parts is investigated using powder produced by water and gas atomization. By using water-atomized 316L powder, compared to gas-atomized powder, more oxide precipitates were introduced into the microstructure with the intent to enhance the strength of the material, as an alternative path to oxide dispersion strengthened materials. The results showed that oxide precipitation was homogenous, with higher-number densities of oxides in the sample built using the water-atomized powder. The oxides were observed to be amorphous and enriched in Si and Cr. The average size of the oxides was ~56 nm. After an annealing heat-treatment at 900 °C, the oxides were observed to remain within the microstructure with only minor changes in size and composition. Mechanical testing at room temperature and at elevated temperature did not show any increase in strength relative to the sample built using gas-atomized powder. However, it was shown that the use of water atomized powder in the L-PBF process provides a viable method of introducing and tailoring the number of oxide particles within a built component relative to a conventional gas atomized powder.

1. Introduction

Powder has a significantly higher surface area relative to its bulk counterpart, which is both to their advantage (sintering activity, flowability) and to their disadvantage (tendency to oxidize). Thus, using powdered materials in a process will result in the component tending to have a higher final oxygen content relative to a cast or machined part. While the higher oxygen content is often considered detrimental to the performance of the component, this inherent property can be used to its benefit. An example is oxide dispersion strengthening (ODS), in which the oxides provide strength to the material [1].

Oxide dispersion strengthening is a method of increasing the mechanical strength of certain materials by homogenously distributing thermally stable nano-sized oxides in the matrix. As compared to precipitation hardening, dispersion strengthening consists of thermally stable, nanosized and insoluble particles designed to hinder dislocation movement, and the volume fraction of particles is usually within 3–4 vol% [2]. The particles interact with the dislocations through multiple interaction mechanisms: through Orowan bowing [3,4], through the climb mechanism, which occurs at higher temperatures [5,6] or interaction with glide dislocations [7]. This, together with the additional grain-pinning effect of the particles, makes this group of materials suitable for high-temperature applications, especially ones in which high temperature strength is required. Oxide dispersion strengthening steels, specifically ferritic and martensitic grades, have been researched and investigated for use in nuclear applications due to their excellent thermal conductivity, thermal expansion coefficient and damage tolerance to neutron irradiation [1,8]. Regular Cr steels, with similar applications, have their temperature limit at 550–600 °C, while the ODS steels are intended to be used at up to 800 °C [8,9]. The microstructures consist of a ferritic/martensitic matrix with a very fine dispersion of Y_2O_3 or Y—Ti oxides [10–12]. The optimal size ranges of the oxides are in the range of 2–5 nm, whereas larger precipitates have been shown to decrease the strengthening effect due to loss of coherency [1,12].

However, ODS alloys have a complex processing route. Alloy powder is first mixed with Y_2O_3 and ball milled for extensive periods of time to allow for the dissolution of Y_2O_3 into the alloy powder. The powder is then canned, degassed and hot-extruded into a stock bar. The extruded bar is heat treated, machined, either cold or hot rolled and then given a final heat treatment [9]. The extensive processing allows

* Corresponding author at: Department of Industrial and Materials Science, Chalmers University of Technology, Rännvägen 2A, SE - 412 96 Gothenburg, Sweden.
E-mail address: riabov@chalmers.se (D. Riabov).

https://doi.org/10.1016/j.matchar.2020.110582
Received 11 May 2020; Received in revised form 17 August 2020; Accepted 18 August 2020
Available online 21 August 2020

for a fine precipitation of the oxide species, but at a hefty cost and with a limited ability to scale-up the production [13]. There is therefore a push to find alternative methods of producing ODS alloys.

An alternative method was explored by Walker et al. [14], who processed a mechanically alloyed ODS powder (of the alloy PM2000) using laser powder bed fusion (L-PBF) to build thin walls. The results showed that homogenous oxide precipitation had occurred within the matrix, and Y_2O_3 could be retained within the material. However, the size distribution was somewhat coarser in the printed material (~50 nm) compared to a conventionally processed PM2000 (~30 nm). No mechanical performance data was provided in that study. The same group also reported some refinement of oxide sizes with higher laser scan speeds, suggesting that melt pool life-time and rapid solidification rates affect the precipitate size. These efforts were further elaborated by Boegelein et al. [15,16], who studied the same material. This time, the samples were mechanically tested and further heat-treated as an attempt to optimize the size distribution as compared to a conventionally processed PM2000 tube. The heat-treatment caused some Ostwald ripening but also precipitation of additional new oxides in the size range of ~10 nm, suggesting that some yttrium and oxygen was still in supersaturation. These precipitates also increased the mechanical strength of the material to be on par with a recrystallized PM2000 tube, however, the as-extruded PM2000 tube was still around 300 MPa stronger. Furthermore, a difference in the precipitate size was noted when comparing thin walls (~17 and ~25 nm) with bulk specimens (~35 nm), thus the oxide distributions shifted toward larger sizes in bulk specimens. Zhong et al. [17] processed ball milled 316L powder with varying contents of Y_2O_3 and of different Y_2O_3 pre-cursor sizes using L-PBF. It was shown that the resulting Y_2O_3 distribution was between 10 and 70 nm and did not seem to be affected by the pre-cursor size. Additionally, it was suggested that the strong convective currents of the melt pool are responsible behind the Y_2O_3 dispersion. The mechanical performance increased by ~30 MPa as compared to a reference 316L powder. Similar findings were provided by Ghayoor et al. [18].

A different approach was conducted in the study of Springer et al. [19], in which a gas atomized 316L powder was processed by laser metal deposition without any shielding gas, causing oxidation of the melt-pool. The microstructural analysis of the built parts showed internal oxidation with microstructures similar to those of ODS alloys. However, the size of these oxides in the as-built condition was around 400 nm, and oxide population was too coarse to have a strengthening effect. Haines et al. [20] had a similar approach, in which a Fe-Cr-Al-Ti stainless steel alloy powder was processed in oxidizing atmospheres using L-PBF. The results showed that when using 100% CO_2 gas Al and Ti were preferentially oxidized, forming oxide precipitates with an average size of 40 nm. Furthermore, it was shown that the precipitates caused a 20% increase of the compressive yield stress at 800 °C compared to a sample processed in Ar gas.

This study therefore investigates a novel approach of synthesizing ODS alloys in-situ within the L-PBF process by using water atomized powder. This approach makes it possible to introduce oxygen contents that are found in conventional ODS alloys (between 0.15 and 0.25 wt% [1]) through the powder alone, circumventing the complexity of mechanical alloying or relying on the atmosphere–melt pool interactions for the oxygen pick-up. However, it is still not well understood how powder surface oxide particulates behave in the L-PBF melt pool, and whether they can produce fine, homogenous oxide distributions within the component. Part of the solution lies in understanding the mechanism of how the oxides transform from the powder surface to an L-PBF processed component and which factors influence the precipitation behavior.

2. Experimental

The investigated materials were two types of stainless steel alloy

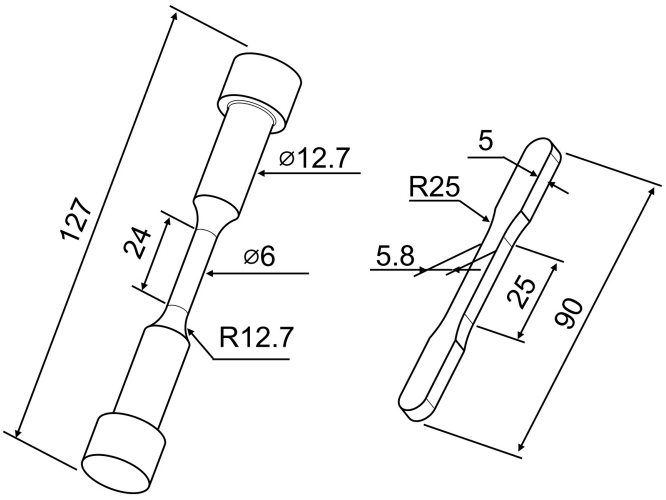

Fig. 1. Tensile specimen geometries for high temperature to the left and for room temperature to the right.

Table 1
Chemical composition of the analyzed powders GA and WA in weight percent, Fe balance.

Powder	O	N	Si	Cr	Ni	Mn	Mo	Ti	Nb	Al
GA	0.07	0.14	0.70	16.6	12.4	1.5	2.5	0.00	0.01	0.02
WA	0.24	0.04	0.80	16.9	12.7	0.2	2.2	0.01	0.04	0.01

Table 2
Particle size distributions of the analyzed powder.

Powder	x_{10} (μm)	x_{50} (μm)	x_{90} (μm)
GA	26.1	42.2	63.3
WA	25.8	46.5	70.4

316L powder provided by Höganäs AB, Sweden. The powder was produced by water atomization and nitrogen gas atomization, and provided in the sieve fraction of 20–53 μm. The particle size distribution was measured by laser diffraction using a Sympatec HELOS instrument. The chemical composition of the two powders was measured by inductively coupled plasma–optical emission spectrometry (ICP-OES) using a SPRECTRO ARCOS, and the interstitial elements (C, O, N and S) were measured by combustion gas analysis using LECO ON836 and CS844 instruments. The powder surfaces were further investigated in a scanning electron microscope (SEM), Leo Gemini 1550.

All specimens were printed using an EOS M290 machine and equipped with a 400W Yb-fiber laser system. The standard printing parameters using a 20 μm layer thickness as provided by the hardware supplier (EOS GmbH) were used to build samples from both powder grades. Prior to printing, the chamber was flushed with argon until a measured oxygen content of 0.1% was reached, upon which the process started. Cubes of 10 × 10 × 10 mm^3 were printed for microstructural evaluations together with samples for mechanical testing. Long rods were also added to the built plate, which allowed changes in bulk oxygen content to be tracked (the same compositional measurement was used as for the powder analysis). A number of samples were heat treated at 900 °C for 1 h in a low vacuum followed by gas quenching (nitrogen at 200 kPa) in a vacuum furnace (ECM FULGRA Duo) to investigate the temperature stability of the microstructures.

The specimens were removed from the build plate and sectioned both in and perpendicular to the building direction. The sectioned samples were mounted in a bakelite resin and polished according to standard Struers procedure for the 316L samples. An initial SiC grinding

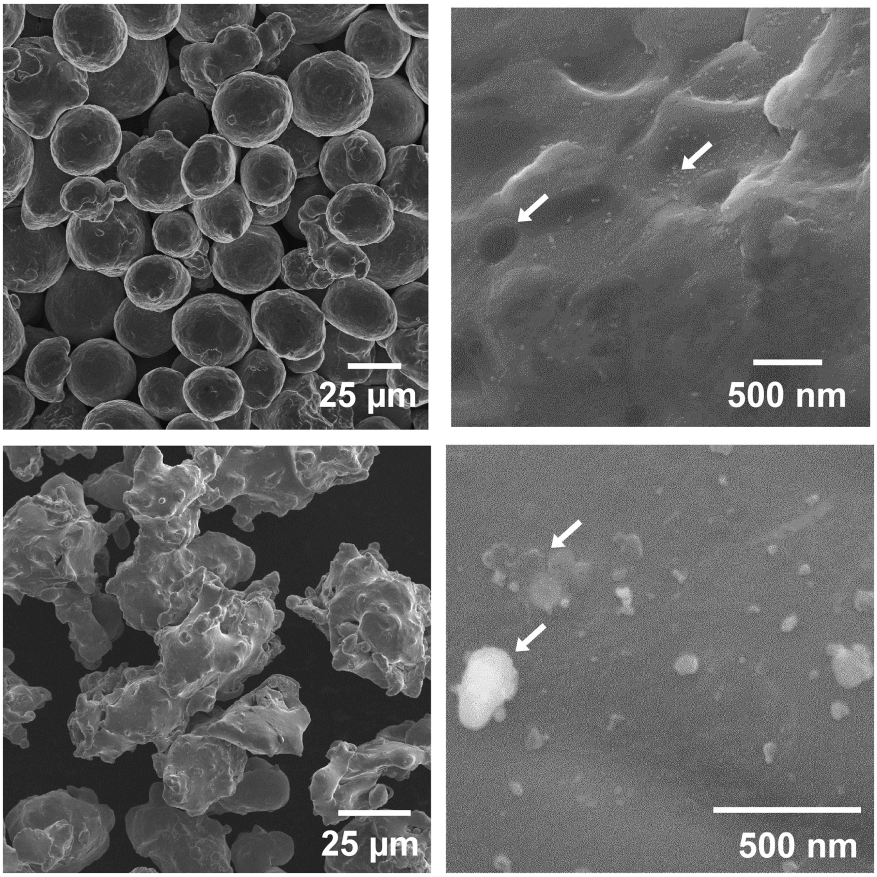

Fig. 2. SEM micrographs of the studied powder in overview (left) and in detail (right). Top, GA. Bottom, WA. The arrows indicate the oxide particulates on the powder surface.

using 500 grit paper was followed by fine grinding using a 9 μm diamond suspension for 5 min, which was followed in turn by polishing using 3 μm diamond suspension for 9 min and by a finishing polish using 0.25 μm colloidal silica for a duration of 5 min. Between the steps, the samples were cleaned in an ultrasonic wash. The built specimen densities were measured using light optical microscopy, Zeiss Imager M2M, on cross-sections transverse to the building direction, which were post-processed using the software imageJ. The samples were then electrolytically etched using a 10 vol% water-based solution of oxalic acid at 3 V DC and further studied using light optical microscopy. Samples for transmission electron microscopy (TEM) were prepared from sectioned 1 mm vertically oriented thick slices, which were thinned mechanically on SiC paper to a thickness of approximately 100 μm. Disks 3 mm in diameter were then punched out from the thinned strip and electrolytically twin-jet polished using a Struers Tenupol-5 until a hole appeared. The etchant was a 10 vol% perchloric acid solution, which was cooled to a temperature of −30 °C.

Thin-foil samples were investigated in an FEI Titan TEM operating at 300 kV and equipped with an EDAX X-ray detector. High-angle annular dark field (HAADF) and bright field (BF) imaging modes using the scanning transmission electron microscopy (STEM) mode were used to capture images of the oxide particulates. Energy-dispersive X-ray spectroscopy (EDX) was used to analyze the chemical composition of the individual particles. The size of the particles was determined by counting > 200 particles per sample. High-resolution TEM (HRTEM) was used to investigate the crystallographic orientation of the oxide particles by bringing the sample into its zone axis, such that individual atom columns were visible, and diffraction patterns were acquired through fast Fourier transformations (FFT) of areas of interest. The TEM samples were also analyzed in the SEM for particle number counts in order to image only the oxides that are truly at the polished surface plane and to probe as little of the volume as possible.

Mechanical testing at room temperature was performed according to the ISO 6892-1 standard using a Zwick Z100, testing a total of seven net-shape specimens. Tests at elevated temperatures were performed using an Instron 8032, equipped with a split furnace. The sample geometries are provided in Fig. 1. Temperature was measured using a contact thermocouple placed directly on the sample. The test specimens were kept at 550 °C for 1 h prior to being pulled. Three samples per powder were machined from as-built cylinders and tested. All testing trials were conducted on vertically oriented samples.

3. Results

3.1. Powder

Considering the importance of the minor alloying elements on the formation and nucleation order of nano-sized oxide particles, a detailed chemical analysis of both powders is provided in Table 1. The chemical analysis shows that the WA and GA powders have a rather similar composition. The Mn and N content was observed to be lower in the WA grade compared to the GA powder. The Mn content is commonly adjusted to lower amounts to accommodate for the strong oxidation when using water as the atomizing medium. A higher oxygen content was present in the WA powder. Table 2 presents results from the particle size measurements of the analyzed powder.

Fig. 2 presents micrographs of the studied powder, with the higher magnification highlighting the surface oxide morphologies. The GA powder seemed to have two oxide populations: larger spherical oxides with a dark contrast and an average size of 200–300 nm and smaller oxides sized up to 50 nm that appeared with a brighter contrast. The smaller particulates appeared more frequently on the surfaces. Other

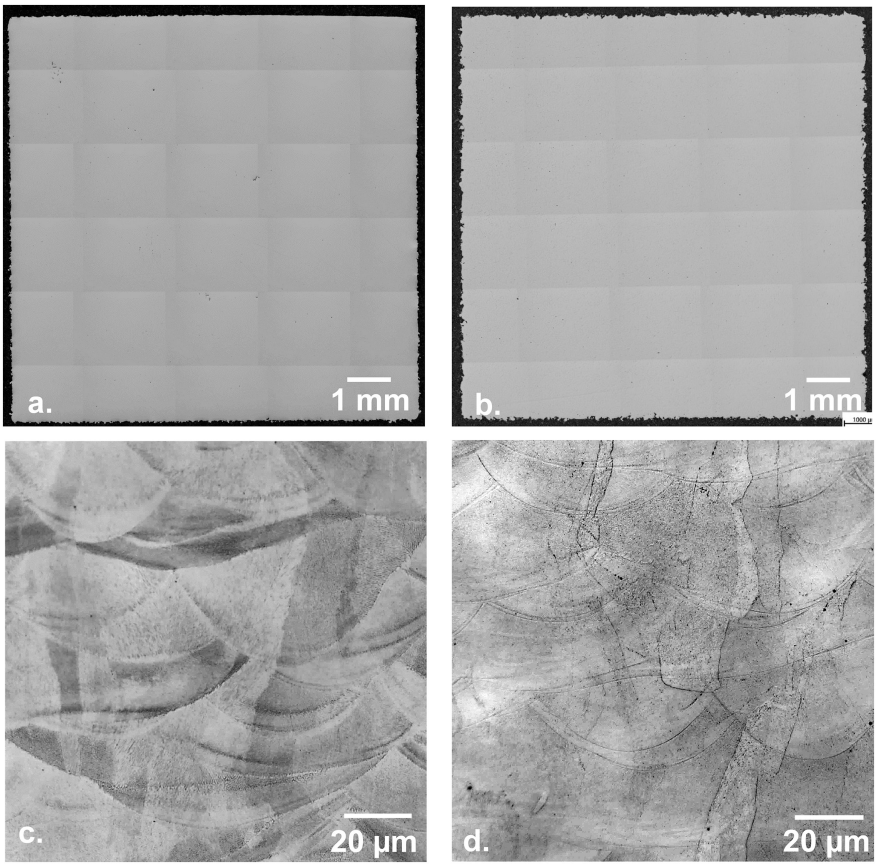

Fig. 3. Light optical images of printed cubes from a, c) the GA sample and b, d) the WA sample.

Table 3
Chemical analysis of built cubes in weight percent and oxygen loss relative to initial oxygen content in the powder.

Sample	Oxygen [wt%]	Oxygen loss
WA	0.17	29%
GA	0.05	28%

oxide morphologies such as splats were also observed, though less frequently. The WA powder was decorated with irregular particulates of varying sizes up to 300 nm, and all the observed oxides appeared with a bright contrast. Splats, similar to the GA powder, were also observed on the surfaces of the WA powder.

3.2. As-built microstructures

Fig. 3 presents polished cross-sections transverse to the building direction of the printed cubes. Both cubes had a final printed density of at least 99.5%. The etched microstructures in the building direction, observed in the same figure, showed microstructures that were typical for L-PBF, with visible melt pools and highly elongated grains. The microstructures of both materials were found to be very similar, and thus, the compositional differences did not show any effect on the microstructure characteristics.

Table 3 shows the chemical analysis of the completed builds. Some oxygen removal had occurred, and the fraction of oxygen loss was similar for the two samples. However, most of the oxygen had remained within the built part and may contribute to an enhanced number density of oxide particles in the WA sample.

3.3. Characterization of oxide inclusions

3.3.1. Microstructure characterization in the as-built state

To fully understand the mechanism of oxide transition from powder to the built part, a detailed characterization of the oxide inclusions within the microstructure was performed. Bright field images from the TEM analysis are displayed in Fig. 4 and show the oxide distribution within the samples. In addition to the oxides, typical L-PBF cell boundaries are visible, with a dark contrast and a grain boundary is visible in the GA sample. The oxides were observed to be fully spherical and distributed homogenously throughout the samples. There was no observed aggregation or segregation to grain boundaries, cell boundaries or any free surfaces. There also appeared to be two different oxide populations in both samples, one population with a bright contrast and the other dark. Hence, these two populations were characterized separately. Within both samples, several oxides with a core-shell structure were observed. This type of arrangement was, however, more frequently observed in the WA sample. Within the core-shell structures, the core always had a darker contrast relative to its shell, as shown in Fig. 4(d). The average size of the oxide particles in the WA sample was 56 ± 27 nm. The bright particles were marginally finer than the dark particles – 52 and 61 nm respectively. The GA sample had finer oxide precipitates than the WA grade, with an average size of 46 ± 25 nm. Similarly, the bright particles were finer in this sample than the darker ones – 42 and 49 nm, respectively. The number density of particles was counted manually. This time, no differentiation between the particles was made, and an average of 1.6×10^7 and 1.3×10^7 mm^{-2} for the WA and GA samples were measured, respectively. There were large variations in the number density in case of the WA samples, with areas having particle densities up to 5.6×10^7 mm^{-2}; see Fig. 5. Such areas seemed to be randomized, without any observed preferential locations. These variations were not observed in the sample produced using the

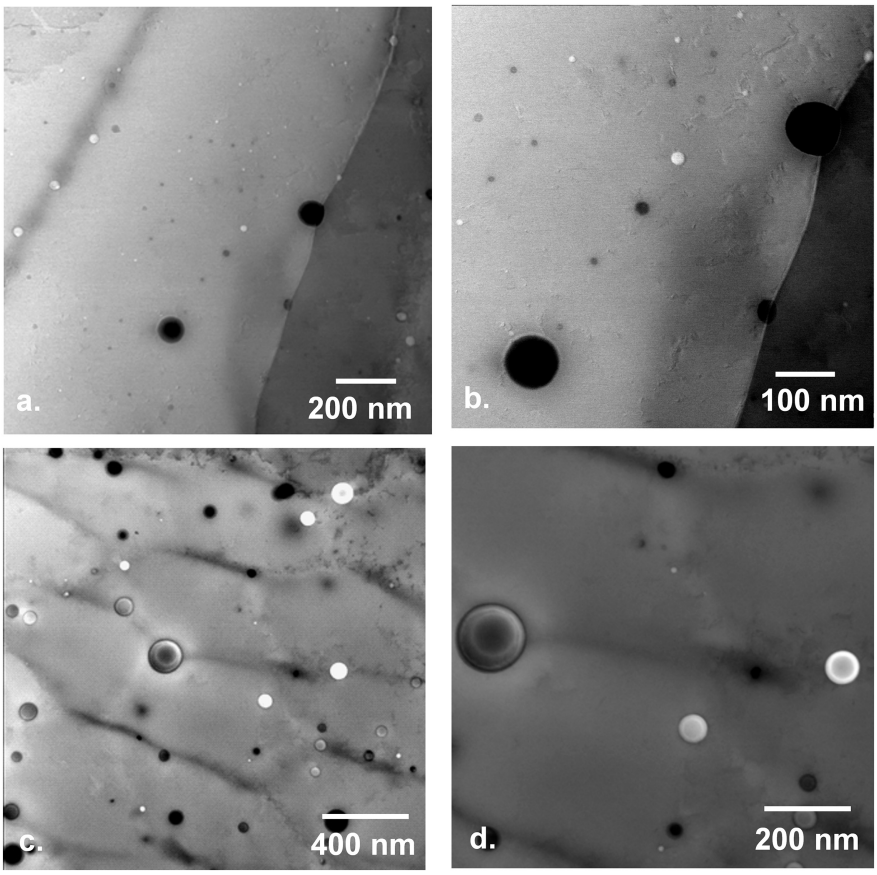

Fig. 4. TEM micrographs from a, b) the GA sample and c, d) the WA sample in the as-built condition.

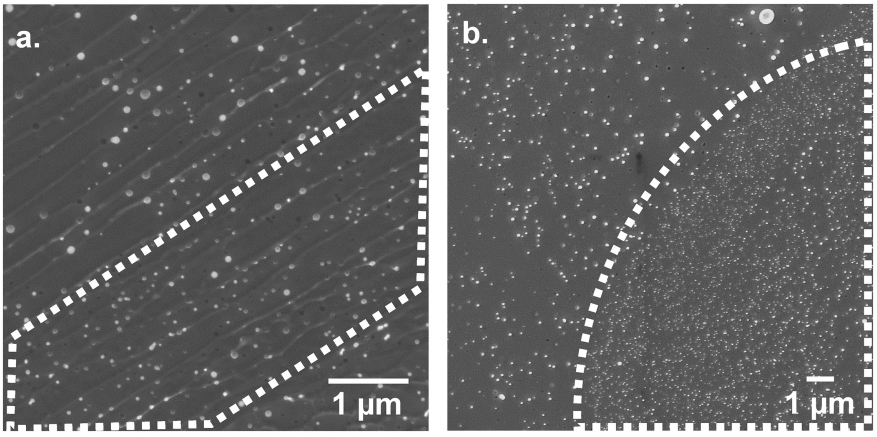

Fig. 5. SEM micrographs of thin foils, exhibiting areas with a higher number density of oxides in the WA sample, a) as-built and b) heat-treated.

GA powder.

To determine the structure of the oxides, a series of selective area diffractions was acquired. The selective area diffraction patterns revealed that the oxides were amorphous. More high-resolution investigations of the core shell structure, where the sample was brought into the zone-axis of the instrument, showed that both components in the core-shell structure were amorphous; see Fig. 6. However, extended beam irradiation during EDX measurements (using higher currents and long focused exposures) caused the onset of crystallization, suggesting that the amorphous structure was meta-stable.

3.3.2. *Microstructural characterization of the annealed samples*

To investigate the temperature stability of the oxides, the samples were heat treated at 900 °C for a duration of 1 h. Like the as-printed samples, the oxides were measured and counted with respect to their number density. Bright field TEM images of the oxides are provided in Fig. 7. The core-shell structure of the WA oxides was still present after the heat-treatment. The average size of the particles was slightly reduced in both the GA and the WA sample, relative to the as-built condition. In the GA samples, the average particle size was 42 ± 23 nm and in WA 47 ± 26 nm. The counted number densities for the WA and the GA samples were 1×10^7 mm^{-2} and 0.9×10^7 mm^{-2}, respectively. Seemingly, the number density of the number of particles was also reduced after the heat treatment. Furthermore, many of the oxides were no longer fully spherical as was observed in the as-built state, and the well-defined interface was replaced by a diffuse border; see Fig. 8.

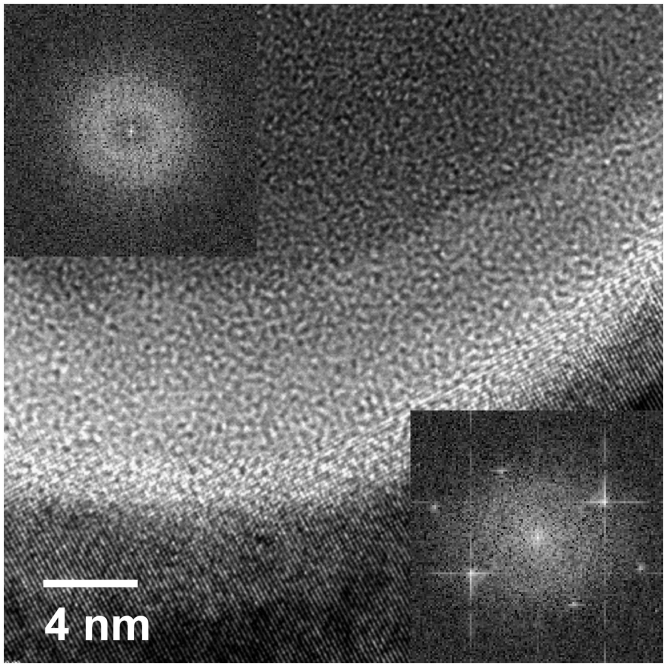

Fig. 6. HRTEM image of core-shell oxide particle. Insets display the FFT of matrix and the oxide particle; the diffuse ring shows that the oxide core was amorphous.

HRTEM images showed that small crystallites had formed within the oxide particles of the WA sample; see Fig. 8. The GA sample also had similar oxide features, with the addition that small oxide particles (around 10 nm) had fully crystallized. Moreover, the cellular substructure was no longer visible in any of the annealed samples. A summary of the oxide particle characteristics in both the as-built and annealed states are presented in Fig. 9.

3.3.3. Composition of the oxide inclusions

To determine the chemical composition of the oxides in the samples, EDX line scans were carried out on thin foils, with the results presented in Fig. 10. The WA sample contained a mixed Cr—Si oxide, with some trace elements of Ti and Mn. As mentioned earlier, some of the oxide constituents were found to be of a core-shell structure, and the line scans indicated that the core was richer in Cr, while the shell was predominantly rich in Si. The findings were found to be consistent throughout the microstructure. The inclusions in the GA sample, however, were mostly formed by a Si rich oxide, with traces of Mn and Al, with an atomic oxygen–to–metal ratio of 3:1. Contrary to the WA sample, no Cr was detected. Additionally, no other oxide types were detected.

To determine the difference between the bright and dark oxides, EDX line scans were performed on the different oxide species to determine whether they were compositionally different. The measurement was performed on the WA sample in the as-built conditions, with the results presented in Fig. 10(c). A compositional variation was detected, and the dark particles were found to be enriched in similar elements to the bright particles, though also containing Fe, Cr and Ni in decreasing amounts. A similar analysis was conducted on the GA sample (not shown here). Although the general oxide composition was shown to be different, the variance between bright and dark particles was similar of the WA sample, and seemed to be systemic. Thus, the bright oxide particles showed enrichment of a few strong oxide-forming elements, especially Si and Cr, and fully depleted in the matrix elements, while the dark oxide particles seem to have more of the matrix elements present.

The chemical composition of the oxides was verified again after the annealing heat-treatment to see whether chemical composition changes had occurred. Line scans were performed on several particles, and the results can be seen in Fig. 11. The results showed some changes in the oxide inclusion composition, an enrichment in Mn in the case of the GA sample and a close to equimolar content of Cr and Si in the case of the WA sample.

3.3.4. Mechanical testing

The GA and WA samples were tested in the as-built condition under uniaxial strain at both room temperature and at an elevated temperature of 550 °C, and the results are presented below in Fig. 12. At room temperature, the GA sample displayed high yield strength (YS) values relative to the WA sample at 601 ± 19 and 504 ± 11 MPa for the GA and WA samples, respectively. The ultimate tensile strength (UTS) followed the same trend with measured values of 727 ± 3 and 644 ± 5 MPa, for the GA and WA samples, respectively. However, both samples showed similar values of elongation at fracture. While at elevated temperatures the difference between the two samples was smaller than during room temperature testing. With the GA and WA samples showing YS values of 381 ± 3 and 346 ± 1 MPa and, UTS values of 468 ± 3 and 417 ± 2 MPa, respectively.

4. Discussion

The intent of this study was to increase the number density of oxides within the microstructure to the point at which the mechanical strength of the component would increase due to an oxide dispersion strengthening mechanism. A brief summary of the oxide characteristics is provided in Table 4.

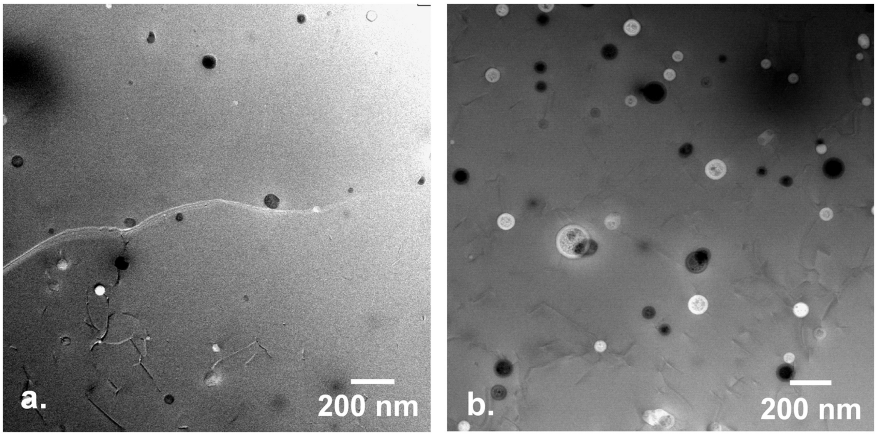

Fig. 7. STEM BF images of annealed samples – a) GA and b) WA.

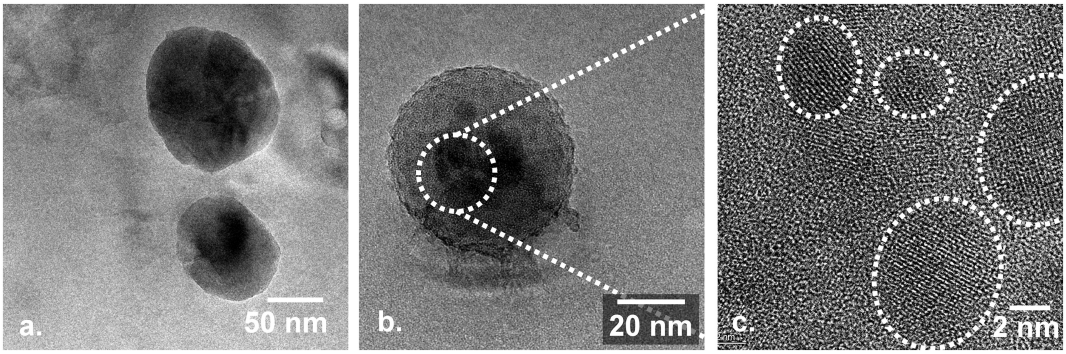

Fig. 8. HRTEM BF image of oxide particles in a) the GA sample and b) the WA sample after annealing. The interface between the oxide and the matrix had become irregular. c) Small crystallites were observed within the oxide particles of the WA sample, as highlighted with dashed circles.

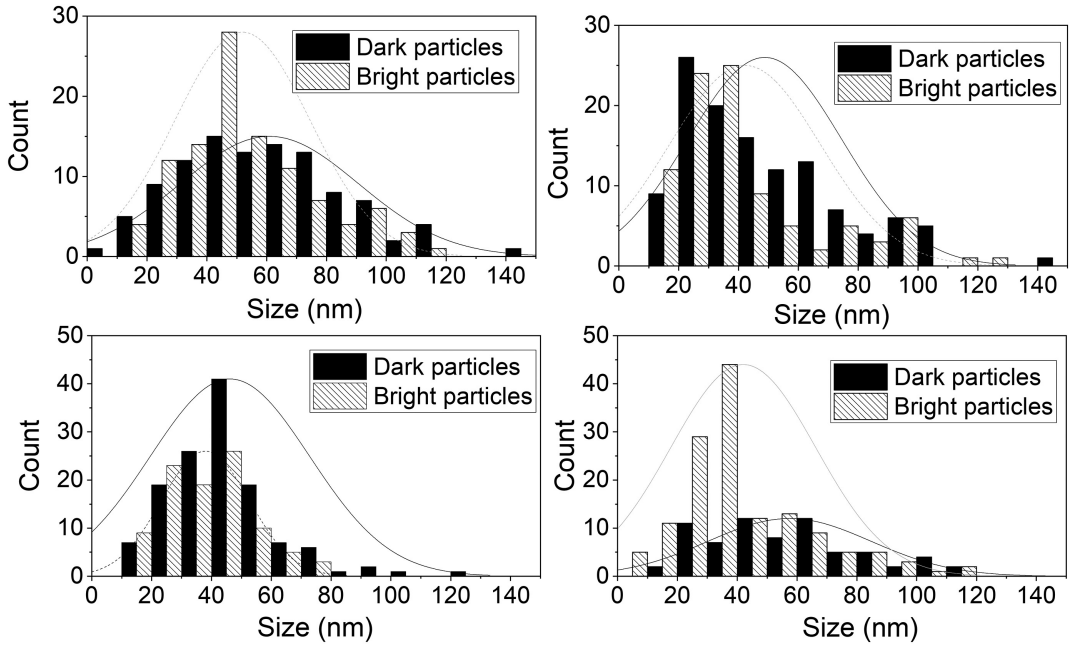

Fig. 9. Summary of particle measurements of as-built (top row) and annealed (bottom row) samples. Left, GA. Right, WA.

Based on the results, the use of the WA powder in the L-PBF process provides a viable method of introducing and tailoring the number of oxide particles within a built component relative to a GA powder. The observed mean number density of the oxide particulates increased from 1.3 10^7 in the GA sample to 1.6·10^7 in the WA sample. However, this increase is relatively low considering that the WA powder introduces roughly three times the amount of oxygen into the process, although the final oxygen content in the built part was found to be 0.17 wt%. Hence, a third of the total oxygen was lost during processing, which is typical for L-PBF [21] and is believed to be due to oxide dissociation, selective evaporation, spatter ejecting or the combination of these [20]. Even at 0.17 wt% of oxygen, a sufficient number density can be achieved, as conventional ODS alloys contain between 0.15 and 0.25 wt % [1]. Another factor that heavily influences the number density is the size factor of the oxides, as the radius of a sphere has a cubic relation to the volume. Hence, even a small increase in the oxide size (46 and 56 nm, for the GA and WA samples, respectively) can drastically reduce the number density of the oxides. That said, areas with number densities up to five times higher were observed within the microstructures of the WA sample. The reason for this variance is still not well understood, whether it originates from the L-PBF processing or whether the variations in the powder feedstock can cause this.

The size difference between the GA and WA samples can be hypothesized to be due several factors, such as the size difference in oxide particulates found on the two powders, the composition of the particulates, the amount of oxygen in the melt pool and the processing conditions. Since the processing conditions were identical, this factor can be ruled out. The size of the oxide particulates found on the GA powder were observed to be of two populations, one with an average size of around 50 nm and the other with an average size of around 200 nm. The WA powder had a wider size distribution of oxide particulates, up to 500 nm, with a higher surface coverage relative to the GA powder. In the built samples, the majority of the oxides were around 50–60 nm, with the top end of the distribution at around 100 nm. Hence, the larger oxide particulates did not seem to carry over to the built sample, nor were any bi-modal distributions previously seen on the powder observed in the GA sample after processing. It is possible, however, that the larger particulates melt when the laser forms a melt-pool, as silica melts at approximately 1700 °C [22] and complex metal silicates at even lower temperatures [23], and due to the strong convective currents in the melt-pool the particulates are dispersed into smaller oxides. Furthermore, the results showed a clear spheroidization of the particulates after processing, especially in the case of the WA powder, in which the particulates were highly irregular. It is therefore likely that the particulates undergo a transition during processing, causing the observed redistribution of oxides.

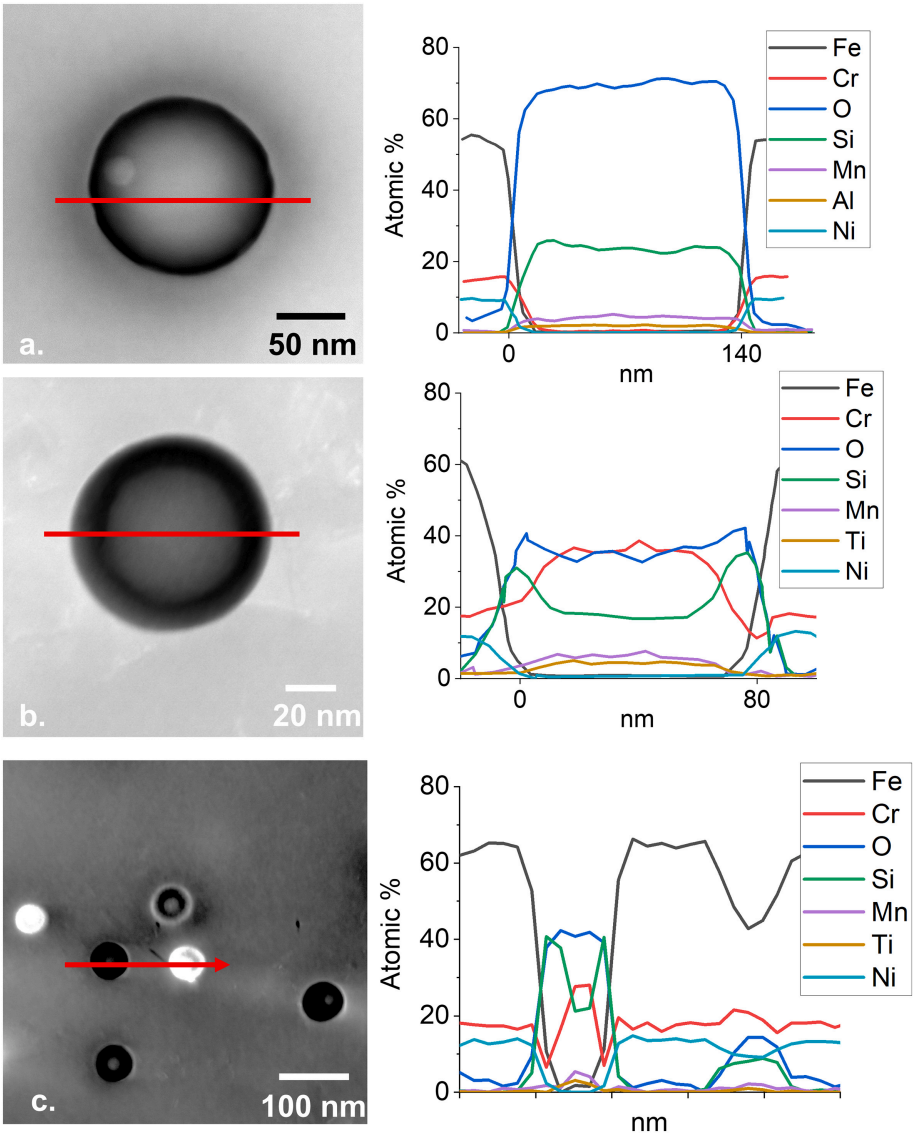

Fig. 10. STEM HAADF EDX line scans and point analysis of oxides found in as-built specimens: a) GA, b) WA and c) WA with two different oxide types analyzed (the contrast in HAADF is inverse relative to the BF).

A change in the composition of the oxides relative to the particulates on the powder surfaces was observed as well. Previous studies [24–26] performing detailed surface characterization on similar powder showed that the oxide particulates on a GA powder are enriched in Cr and Mn, with minor concentrations in Si. The exact composition varies according to several factors, although the oxidation of Si is negligible unless the atomizing gas is extremely lean on O_2 [25]. Hence, even when using high-purity gases, the oxide particulates are expected to contain the elements Mn, Cr and Si. However, the results showed that after L-PBF processing, the oxides contained a surprisingly high fraction of Si (Mn and Al were found in minor fractions), indicating a transformation relative to the powder particulates. In the case of the WA powder, studies on fine powder fractions [24,27,28] of stainless steel powder point toward a strong tendency for Si to oxidize during atomization. Hence, the major constituent in the surface oxide particulates is Si, with minor fractions of Cr and traces of Mn, and the oxides after L-PBF processing were found to contain Cr and Si. It is therefore more difficult to draw conclusions as to whether oxide transformation occurs based on the chemistry in the case of the WA sample, since the particulate and oxide compositions were similar. Hence, for the WA sample, the change in morphology provides evidence of transformation, rather than the change in composition. It is possible that the oxide particulates of GA reduce to Si-based oxides during melting, and due to the higher amounts of oxygen in the WA sample, there will be a lack of Si availability and hence Cr remains in the oxide.

It is widely accepted that the L-PBF melt pool reaches very high temperatures, causing selective vaporization of elements and strong convective flows [29,30]. Yan et al. [31] provided thermodynamic simulations of the oxide stabilities of a 316L material, in which it was shown that at equilibrium, all of the oxides dissolve at around 1700 °C. Thus, it is possible that the oxides fully dissolve in the melt-pool. However, due to the very short lifetime of an L-PBF melt-pool, it is possible that the oxide species do not have time to fully dissolve due to relatively slow kinetics of dissolution, resulting in the presence of some oxides in the liquid melt-pool. Gruber et al. [32] showed that during electron beam melting of the alloy 718, a large fraction of such oxide residues can accumulate on the melt surface due to the significantly lower density compared to the molten metal and result in large oxide defects. Literature on the modeling of inclusion formation in welding provides another possible mechanism that can be responsible for the size differences between the GA and the WA samples, namely, oxide collisions in the liquid leading to their growth [33,34]. Hence, it could

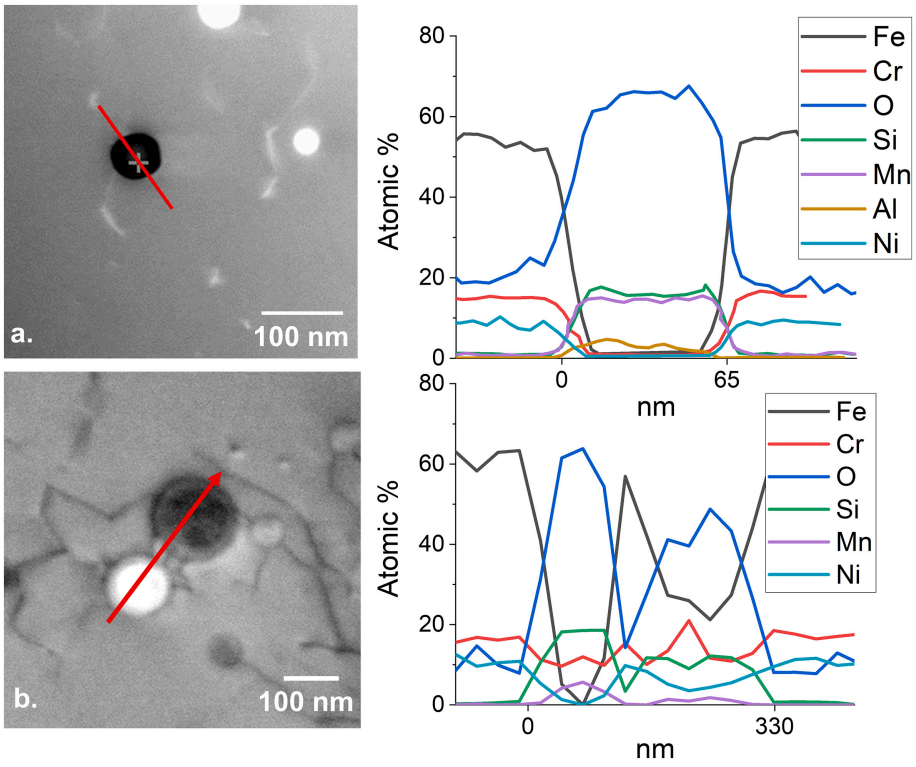

Fig. 11. STEM EDX line scans of oxide particles in the annealed a) GA sample and b) WA sample.

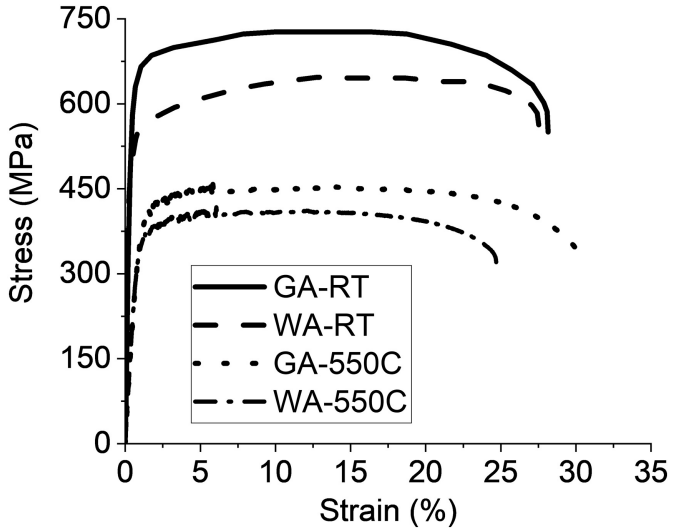

Fig. 12. Mechanical properties of GA and WA at room temperature and at an elevated temperature of 550 °C.

Table 4
Summary of oxide sizes, major and minor elements, and number densities found in the microstructures of the GA and WA samples.

Sample	Mean oxide size	Number density	Major elements	Minor elements
GA	46 ± 25 nm	1.3×10^{7} mm^{-2}	Si	Al, Mn
WA	56 ± 27 nm	1.6×10^{7} mm^{-2}	Cr, Si	Ti, Mn
GA-HT	42 ± 23 nm	0.9×10^{7} mm^{-2}	Si, Mn	Al
WA-HT	47 ± 26 nm	1×10^{7} mm^{-2}	Cr, Si	Ti, Mn

be expected that due to the higher number of particulates in the WA powder, the number of collisions is greater from a probability point of view. Under the assumption that the oxides do not fully dissolve and remain within the melt-pool, this mechanism can possibly lead to the observed larger size of the oxides in the WA sample.

The annealing heat treatment had several effects on the oxides. It reduced the average size of the oxides (see Table 4) and altered the interface between the oxide and the matrix. Additionally, minor compositional changes were noted. These effects were observed in both samples, yet the largest change concerned the oxides of the WA-HT sample. The reduction of the particle size can be explained by two possible mechanisms. Crystallization of the amorphous oxides, which also explains the fuzzy interface after annealing, together with the presence of small crystallites within the still amorphous oxide. Similar crystallites were reported during L-PBF processing of a PM2000 alloy powder in the as-built condition [16]. Another reason for the oxide size reduction can be connected to the tendency to reach an equilibrium state, where the oxygen content reaches approximately 60 at.% (valid for corundum- and quartz-type oxides), with Cr diffusing out from the oxide. Hence, it is believed that no additional oxides precipitate during the heat treatment, but reduction in size and amount is observed, as previously reported in the literature as well [16].

To put the results into context with conventionally processed ODS alloys, the size distribution in this study was not optimized, and oxide particles should preferably be < 10 nm, with high-number densities to fully benefit from the ODS effect [1,9,16]. Additionally, the oxides found in this study were amorphous and incoherent with the parent matrix, as compared to the coherent or semi-coherent Y-Ti-O nano clusters found in modern ODS alloys [12,35–37]. The Cr—Si oxides found in this study also do not have the coarsening resistance or the high temperature stability of the Y based oxides in conventional ODS steels. By converting the number densities reported in this study to three-dimensional values [33], it becomes possible to compare particle densities to the values found in literature. Klueh et al. [1] report of values between 12×10^{20} and 10^{23} m^{-3}, while this study had an observed maximum of 2.8×10^{15} m^{-3}. A part of the difference can be due

to the methodology, yet a gap between the number densities achieved in this study and in the reported ones remains. This, together with the larger sizes of the oxides, explains the lack of a strengthening mechanism observed in this study. Since a large part of the initial strength of ODS alloys comes from the extensive deformation hardening during processing, it was thought that at higher temperatures the dislocations would interact with the oxides in the WA sample. However, the effect was not observed at the obtained oxide particle size and number density.

5. Summary and conclusions

This study investigated the concept of using gas- and water-atomized powder in the L-PBF process to tailor the number density of oxides in order to test the potential of developing an oxide dispersion strengthening mechanism in 316L components produced by L-PBF. The use of a WA powder produced parts equal to the GA powder in terms of density and microstructural characteristics. The oxides were found to be homogenously distributed within the microstructures, having an average size of 46 ± 25 nm and 56 ± 27 nm for the GA and WA samples, respectively. However, even though three times higher initial oxygen content was registered for the WA powder compared to the GA one, the use of WA powder resulted in a number density of oxides of 1.6×10^7 mm^{-2}, compared to 1.3×10^7 mm^{-2} observed in case of the GA sample. Furthermore, the oxides were found to be amorphous in the as-built condition and started to crystallize after the annealing heat treatment, forming small crystallites within the particles. The oxides found in the GA sample were rich in Si, with trace amounts of Mn and Al, while the oxides in the WA sample were rich in Cr and Si, with traces of Mn and Ti. It is suggested that the oxides melt, disperse and partially dissolve during processing, based on the morphological and compositional transformation relative to the particulates found on the initial powder surfaces. No additional strengthening effects from the oxide particles were observed relative to the GA sample during mechanical testing at room and elevated temperatures. By contrast, the UTS was reduced from 727 ± 3 to 644 ± 5 MPa at room temperature and from 468 ± 3 to 417 ± 2 MPa at 550 °C. Hence, further work to increase the number density of the oxide particles and decrease the size through compositional variation of the powder and L-PBF process adjustment is recommended to attain the benefit of oxide dispersion strengthening in L-PBF processed materials. However, the use of the WA powder in the L-PBF process provides a viable method of introducing and tailoring the number of oxide particles within a built component relative to a GA powder.

Data availability

The raw/processed data required to reproduce these findings cannot be shared at this time as the data also forms part of an ongoing study.

Declaration of competing interest

The authors declare that they have no known competing financial interests or personal relationships that could have appeared to influence the work reported in this paper.

Acknowledgements

This work has been conducted in the framework of the Centre for Additive Manufacturing – Metal (CAM^2), supported by the Swedish Governmental Agency of Innovation Systems (Vinnova).

References

[1] R.L. Klueh, J.P. Shingledecker, R.W. Swindeman, D.T. Hoelzer, Oxide dispersion-strengthened steels: a comparison of some commercial and experimental alloys, J. Nucl. Mater. 341 (2005) 103–114, https://doi.org/10.1016/j.jnucmat.2005.01.017.
[2] M.A. Meyers, K.K. Chawla, Mechanical Behavior of Materials, Cambridge University Press Cambridge, 2009.
[3] E. Orowan, Symposium on internal stresses in metals and alloys, Inst. Met. Lond. 451 (1948).
[4] D.J. Bacon, U.F. Kocks, R.O. Scattergood, The effect of dislocation self-interaction on the orowan stress, Philos. Mag. J. Theor. Exp. Appl. Phys. 28 (1973) 1241–1263, https://doi.org/10.1080/14786437308227997.
[5] E. Arzt, D.S. Wilkinson, Threshold stresses for dislocation climb over hard particles: the effect of an attractive interaction, Acta Metall. 34 (1986) 1893–1898, https://doi.org/10.1016/0001-6160(86)90247-6.
[6] J. Rösler, E. Arzt, The kinetics of dislocation climb over hard particles—I. climb without attractive particle-dislocation interaction, Acta Metall. 36 (1988) 1043–1051, https://doi.org/10.1016/0001-6160(88)90158-7.
[7] M.C. Brandes, L. Kovarik, M.K. Miller, G.S. Daehn, M.J. Mills, Creep behavior and deformation mechanisms in a nanocluster strengthened ferritic steel, Acta Mater. 60 (2012) 1827–1839, https://doi.org/10.1016/j.actamat.2011.11.057.
[8] S.J. Zinkle, Fusion materials science: overview of challenges and recent progress, Phys. Plasmas. 12 (2005) 1–8, https://doi.org/10.1063/1.1880013.
[9] S. Ukai, T. Kaito, S. Ohtsuka, T. Narita, M. Fujiwara, T. Kobayashi, Production and properties of nano-scale oxide dispersion strengthened (ODS) 9Cr martensitic steel claddings, ISIJ Int. 43 (2003) 2038–2045, https://doi.org/10.2355/isijinternational.43.2038.
[10] M.K. Miller, E.A. Kenik, K.F. Russell, L. Heatherly, D.T. Hoelzer, P.J. Maziasz, Atom probe tomography of nanoscale particles in ODS ferritic alloys, Mater. Sci. Eng. A 353 (2003) 140–145, https://doi.org/10.1016/S0921-5093(02)00680-9.
[11] I.-S. Kim, J.D. Hunn, N. Hashimoto, D.L. Larson, P.J. Maziasz, K. Miyahara, E.H. Lee, Defect and void evolution in oxide dispersion strengthened ferritic steels under 3.2 MeV Fe+ ion irradiation with simultaneous helium injection, J. Nucl. Mater. 280 (2000) 264–274. doi:https://doi.org/10.1016/S0022-3115(00)00066-0.
[12] M.J. Alinger, G.R. Odette, D.T. Hoelzer, On the role of alloy composition and processing parameters in nanocluster formation and dispersion strengthening in nanostuctured ferritic alloys, Acta Mater. 57 (2009) 392–406, https://doi.org/10.1016/j.actamat.2008.09.025.
[13] F. Bergner, I. Hilger, J. Virta, J. Lagerbom, G. Gerbeth, S. Connolly, Z. Hong, P.S. Grant, T. Weissgärber, Alternative fabrication routes toward oxide-dispersion-strengthened steels and model alloys, Metall. Mater. Trans. A. 47 (2016) 5313–5324, https://doi.org/10.1007/s11661-016-3616-2.
[14] J.C. Walker, K.M. Berggreen, A.R. Jones, C.J. Sutcliffe, Fabrication of Fe–Cr–Al oxide dispersion strengthened PM2000 alloy using selective laser melting, Adv. Eng. Mater. 11 (2009) 541–546, https://doi.org/10.1002/adem.200800407.
[15] T. Boegelein, S.N. Dryepondt, A. Pandey, K. Dawson, G.J. Tatlock, Mechanical response and deformation mechanisms of ferritic oxide dispersion strengthened steel structures produced by selective laser melting, Acta Mater. 87 (2015) 201–215, https://doi.org/10.1016/j.actamat.2014.12.047.
[16] T. Boegelein, E. Louvis, K. Dawson, G.J. Tatlock, A.R. Jones, Characterisation of a complex thin walled structure fabricated by selective laser melting using a ferritic oxide dispersion strengthened steel, Mater. Charact. 112 (2016) 30–40, https://doi.org/10.1016/j.matchar.2015.11.021.
[17] Y. Zhong, L. Liu, J. Zou, X. Li, D. Cui, Z. Shen, Oxide dispersion strengthened stainless steel 316L with superior strength and ductility by selective laser melting, J. Mater. Sci. Technol. 42 (2020) 97–105, https://doi.org/10.1016/j.jmst.2019.11.004.
[18] M. Ghayoor, K. Lee, Y. He, C. Chang, B.K. Paul, S. Pasebani, Selective laser melting of austenitic oxide dispersion strengthened steel: processing, microstructural evolution and strengthening mechanisms, Mater. Sci. Eng. A 788 (2020) 139532, https://doi.org/10.1016/j.msea.2020.139532.
[19] H. Springer, C. Baron, A. Szczepaniak, E.A. Jägle, M.B. Wilms, A. Weisheit, D. Raabe, Efficient additive manufacturing production of oxide- and nitride-dispersion-strengthened materials through atmospheric reactions in liquid metal deposition, Mater. Des. 111 (2016) 60–69, https://doi.org/10.1016/j.matdes.2016.08.084.
[20] M.P. Haines, N.J. Peter, S.S. Babu, E.A. Jägle, In-situ synthesis of oxides by reactive process atmospheres during L-PBF of stainless steel, Addit. Manuf. 101178 (2020), https://doi.org/10.1016/j.addma.2020.101178.
[21] C. Pauzon, E. Hryha, P. Forêt, L. Nyborg, Effect of argon and nitrogen atmospheres on the properties of stainless steel 316L parts produced by laser-powder bed fusion, Mater. Des. 179 (2019) 107873, https://doi.org/10.1016/j.matdes.2019.107873.
[22] W.M. Haynes, CRC Handbook of Chemistry and Physics, 92nd Edition, Taylor & Francis, 2011, https://books.google.co.cr/books?id=MpV5tQEACAAJ.
[23] M. Tanahashi, N. Furuta, C. Yamauchi, T. Fujisawa, Phase equilibria of the MnO-SiO2-CrOx system at 1873 K under controlled oxygen partial pressure, ISIJ Int. 41 (2001) 1309–1315, https://doi.org/10.2355/isijinternational.41.1309.
[24] Y. Hedberg, M. Norell, J. Hedberg, P. Szakálos, P. Linhardt, I. Odnevall Wallinder, Surface characterisation of fine inert gas and water atomised stainless steel 316L powders: formation of thermodynamically unstable surface oxide phases, Powder Metall. 56 (2013) 158–163, https://doi.org/10.1179/1743290112Y.0000000041.
[25] L. Nyborg, M. Norell, I. Olefjord, Surface studies of powder metallurgical stainless steel, Surf. Interface Anal. 19 (1992) 607–614, https://doi.org/10.1002/sia.7401901113.
[26] I. Olefjord, L. Nyborg, Surface analysis of gas atomized ferritic steel powder, Powder Metall. 28 (1985) 237–243, https://doi.org/10.1179/pom.1985.28.4.237.
[27] I. Nyborg, T. Tunberg, P.X. Wang, Surface product formation during water atomization and sintering of austenitic stainless steel powder, Met. Powder Rep. 45 (1990) 750–753, https://doi.org/10.1016/0026-0657(90)90459-T.

[28] T. Tunberg, L. Nyborg, Surface reactions during water atomisation and sintering of austenitic stainless steel powder, Powder Metall. 38 (1995) 120–130, https://doi.org/10.1179/pom.1995.38.2.120.
[29] S. Ly, A.M. Rubenchik, S.A. Khairallah, G. Guss, M.J. Matthews, Metal vapor micro-jet controls material redistribution in laser powder bed fusion additive manufacturing, Sci. Rep. 7 (2017) 4085, https://doi.org/10.1038/s41598-017-04237-z.
[30] U. Scipioni Bertoli, G. Guss, S. Wu, M.J. Matthews, J.M. Schoenung, In-situ characterization of laser-powder interaction and cooling rates through high-speed imaging of powder bed fusion additive manufacturing, Mater. Des. 135 (2017) 385–396, https://doi.org/10.1016/j.matdes.2017.09.044.
[31] F. Yan, W. Xiong, E. Faierson, G.B. Olson, Characterization of nano-scale oxides in austenitic stainless steel processed by powder bed fusion, Scr. Mater. 155 (2018) 104–108, https://doi.org/10.1016/j.scriptamat.2018.06.011.
[32] H. Gruber, C. Luchian, E. Hryha, L. Nyborg, Effect of powder recycling on defect formation in electron beam melted alloy 718, Metall. Mater. Trans. A. 51 (2020) 2430–2443, https://doi.org/10.1007/s11661-020-05674-8.
[33] S.S. Babu, F. Reidenbach, S.A. David, T. Böllinghaus, H. Hoffmeister, Effect of high energy density welding processes on inclusion and microstructure formation in steel welds, Sci. Technol. Weld. Join. 4 (1999) 63–73, https://doi.org/10.1179/136217199101537581.
[34] T. Hong, T. Debroy, S.S. Babu, S.A. David, Modeling of inclusion growth and dissolution in the weld pool, Metall. Mater. Trans. B Process Metall. Mater. Process. Sci. 31 (2000) 161–169, https://doi.org/10.1007/s11663-000-0141-9.
[35] M. Klimiankou, R. Lindau, A. Möslang, HRTEM study of yttrium oxide particles in ODS steels for fusion reactor application, J. Cryst. Growth 249 (2003) 381–387, https://doi.org/10.1016/S0022-0248(02)02134-6.
[36] J. Ribis, Y. de Carlan, Interfacial strained structure and orientation relationships of the nanosized oxide particles deduced from elasticity-driven morphology in oxide dispersion strengthened materials, Acta Mater. 60 (2012) 238–252, https://doi.org/10.1016/j.actamat.2011.09.042.
[37] A. Hirata, T. Fujita, Y.R. Wen, J.H. Schneibel, C.T. Liu, M.W. Chen, Atomic structure of nanoclusters in oxide-dispersion-strengthened steels, Nat. Mater. 10 (2011) 922–926, https://doi.org/10.1038/nmat3150.